

Optimization of the structure of an induction motor with magnetic bearings

Hamed Azadrou¹, Reza Ghanizadeh^{2*}

¹ Department of Electrical Engineering, Salmas Branch, Islamic Azad University, Salmas, Iran

² Department of Electrical Engineering, Urmia Branch, Islamic Azad University, Urmia, Iran.

ARTICLE INFO

Article history:
Received: 09 December 2024
Revised: 08 March 2025
Accepted: 09 April 2025

Keywords:

Induction motor
Magnetic bearing
Electromagnetic torque
Levitation force
optimization



Copyright: © 2025 by the authors. Submitted for possible open access publication under the terms and conditions of the Creative Commons Attribution (CC BY) license (<https://creativecommons.org/licenses/by/4.0/>)

ABSTRACT

Although conventional high-speed gas turbines and electric motors equipped with mechanical gearboxes are practical solutions, they face significant environmental constraints and suffer from the inefficiencies associated with mechanical converters. As a result, high-speed electric motors, especially those designed to overcome these limitations, have become increasingly favorable. Bearing-less induction motors (BLIMs) offer notable advantages, including the elimination of friction losses, minimization of wear, reduced maintenance requirements, and the inclusion of an internal monitoring system. However, due to their unique structure and the complex interaction between torque and force winding fields, BLIMs are not well-suited for high-power applications. This research investigates the analytical design of a high-speed BLIM, aiming to enhance performance, efficiency, and torque density. To achieve this, a multi-objective optimization process of the derived dimensions is employed. Furthermore, a finite element analysis of the motor is conducted, and the results are compared with those of a BLIM optimized using a genetic algorithm.


1. Introduction

A bearing-less motor is a distinctive type of motor that employs magnetic bearings, eliminating any direct mechanical connection between its rotating and stationary parts [1]. These motors include additional windings alongside the standard stator windings found in conventional electrical machines, generating the suspension force. Magnetic bearing technology is adaptable to various types of electric motors [2] and [3]. Induction motors are extensively utilized in various industries because of their multiple advantages and can also be modified to operate without bearings. In a bearing-less induction motor (BLIM), two distinct magnetic fields are created to simultaneously generate electromagnetic torque and suspension force. This is typically

accomplished by incorporating separate windings within the same stator slots [4] and [5]. Alternatively, a unified winding configuration can be employed to produce both fields simultaneously, significantly enhancing the motor's torque density [6]-[8]. However, this configuration increases the complexity of the power electronic converter and enhances field interference. To address these issues, a specialized combined winding design has been developed. High-speed electrical machines offer significant benefits across various industries [9]. For instance, earlier research has investigated the development of a high-speed induction motor designed for gas compressor applications [10]-[12]. Another study concentrated on the electrical analysis, magnetic design, prototype development, and initial testing of a high-speed

* Corresponding author

E-mail address: reza.ghanizadeh@iau.ac.ir

 <https://orcid.org/0000-0003-2093-0267>

<http://dx.doi.org/10.48308/ijrtei.2025.237898.1068>

induction motor intended for a small centrifugal compressor [13]-[15]. Furthermore, it has been suggested to utilize medium-voltage synchronous motors, controlled by variable speed drives, in compressor systems [16]-[18]. Furthermore, studies have concentrated on the design and performance evaluation techniques for bearing-less induction motors, highlighting their differences from conventional induction motors [19]. A study presented an improved bearing-less induction motor featuring innovative magnetic slot wedges, resulting in reduced thermal issues and electrical losses [20]. Another design strategy utilized high-speed electrical machines with magnetic bearings and mutual inductances, introducing an innovative fixed-pole rotor structure to reduce interference problems in magnetic bearing motors [21] and [22]. In addition, a seeker optimization algorithm (SOA) has been introduced to optimize real parameters by simulating human search behaviour, and its details have been thoroughly examined in later research [23] and [24]. However, these studies do not focus on the design and optimization of a high-power induction motor specifically designed for bearing-less technology and its performance. In our work, we present an optimized bearing-less induction motor tailored for high-speed gas compressor applications. This motor features a multi two-pole squirrel cage rotor, which improves both suspension and torque performance compared to conventional designs. The initial motor design was developed using analytical methods and subsequently refined through a seeker optimization algorithm.

2. Structure of the proposed BLIM

Designing a BLIM involves many similar stages to those of a conventional induction motor, but it differs significantly due to the inclusion of magnetic bearings. In a BLIM, the stator's slots and windings must be carefully designed to not only produce torque, as in traditional motors, but also to create an electromagnetic force for rotor suspension. This paper focuses on the design and optimization of a three-phase bearing-less squirrel cage induction motor. Within the air gap, there are two distinct magnetic fields: the P_t -pole field, which is similar to that in conventional motors and is referred to as the torque or motor field, and the $P_f = P_t \pm 2$ pole field, known as the force or suspension field. Both of these fields induce currents in the rotor bars.

2.1. Rotor Design

To tackle the problem, a multi two-pole rotor design (MTP_BLIM) is suggested, as shown in Fig. 1. With a two-pole torque field and a four-pole force field present in the air gap, the proposed rotor design is intended to induce only two-pole currents in the rotor. This setup aims to minimize the interaction between the force generation system and the torque. The torque and force characteristics of a BLIM equipped with a standard squirrel cage rotor are illustrated in Fig. 2. These graphs, produced through 3-D finite element analysis (FEA) with ANSYS Electronics, show that as speed increases, the torque remains relatively stable while the force decreases significantly, becoming almost negligible at very high

speeds. This highlights the limitations of the traditional rotor design.

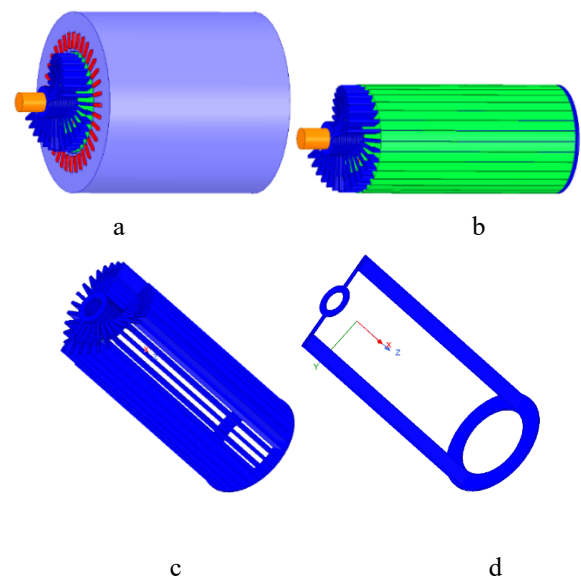


Fig. 1. multi two-pole BLIM, (a) the motor, (b) rotor design, (c) squirrel cage, (d) a two-pole squirrel cage.

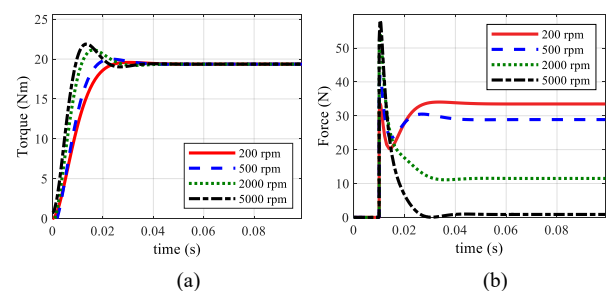


Fig. 2. Electromagnetic torque and force for conventional rotor structure at different speeds, (a) torque, (b) force.

2.2. Stator Design

In a traditional BLIM, the stator has two separate windings located in the same slots, responsible for producing the torque and force fields. An alternative method, called the combined winding, utilizes a single set of windings to generate both fields. While this method results in a higher torque density, the efficiency of the system is greatly diminished due to the non-zero speed-induced voltage in the force windings. To mitigate this problem, a parallel winding configuration, as depicted in Fig. 3, is used [8]. This design features two separate sets of terminals: one dedicated to torque current and the other to suspension force current. These terminals share a common coil, where the torque terminal is connected in such a way that the two identical coil sections are positioned in opposite directions. Consequently, the speed-induced voltage in one force winding is negative while it is positive in the other, thereby canceling out the voltages. This configuration permits independent control of the force current regardless of rotor speed, without requiring isolation from the torque inverter.

Fig. 4 illustrates a comparison between three different winding techniques for various torque poles (P_t) and force poles (P_f), based on data from finite element analysis. As depicted in Fig. 4(a), the DPNV method yields a much

higher torque density than the separated winding (*sep*) and combined winding (*com*) techniques.

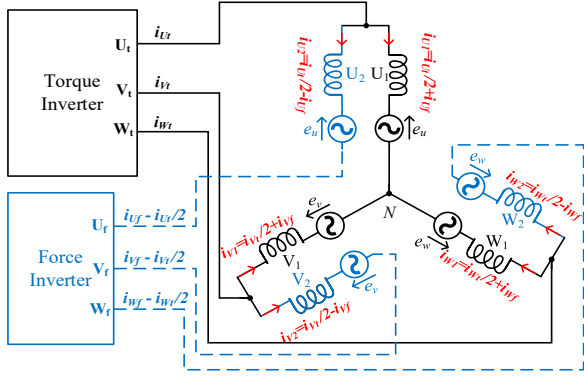


Fig. 3. BLIM with parallel winding structure

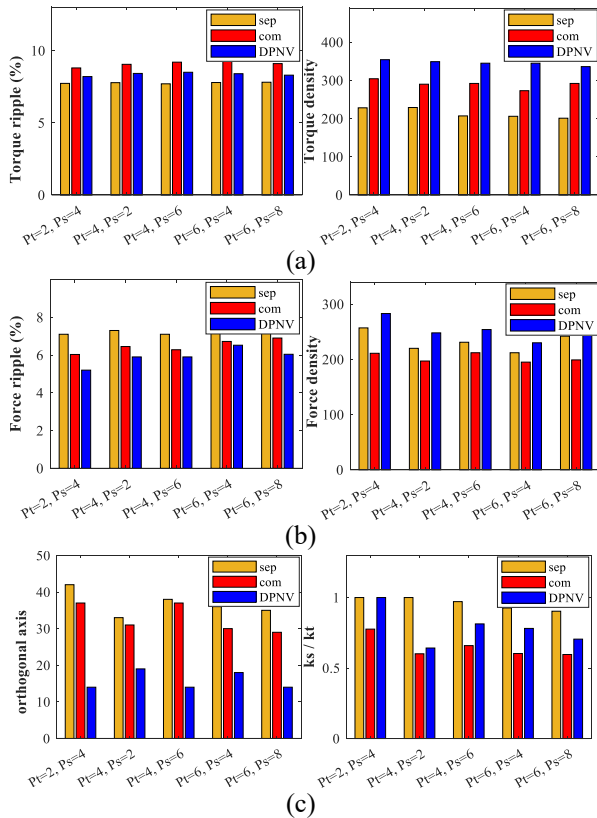


Fig. 4. Comparison of three winding strategies, (a) torque density and torque ripple, (b) force density and force ripple, (c) current efficiency and orthogonal axis factor.

Although the initial motor design shows the proposed method has more torque ripple, this can be reduced by optimizing motor dimensions. Moreover, Fig. 4(b) highlights the DPNV method's superior performance in average force and quality. The force and torque ripples were evaluated under several rotor displacement scenarios from the center. The k_s/k_t ratio demonstrates the efficiency of the machine in converting current into radial forces [12]. Additionally, the orthogonal axis represents the percentage change of force in one axis relative to another, defined in this study as $\Delta F_y/F_x$. Based on the comparison, a BLIM with a DPNV winding configuration has been chosen.

2.3. Mathematical Equations of the BLIM

In this work, the motor design is based on the equations provided in reference [18]. A lower pole number (P_t) results in a higher motor power factor. Additionally, setting $P_f = P_t + 2$ enhances the force capacity by aligning the Lorentz and Maxwell forces [21]. Thus, P_t is chosen as 2 and P_f as 4 for the proposed motor. The current density in the stator windings and the slot fill factor are both kept constant at 4 Arms/mm² and 0.5, respectively. The initial dimensions determined for a 2.2 kW BLIM operating at 30,000 rpm are detailed in Table I. In the following section, various parameters of the BLIM are treated as variables to study their impact on motor performance. A detailed examination of magnetic forces in a BLIM with a squirrel cage rotor can be found in [4]. The magnetic energy is represented by (1).

$$W_m = \frac{1}{2} [i_{ab}]^T [L_{ab}] [i_{ab}] \quad (1)$$

Here, i_{ab} denotes the two-phase current vector, and L_{ab} signifies the inductance matrix [4]. Assuming F_x and F_y are the suspension forces in the x and y directions respectively, these forces can be expressed as the partial derivatives of the energy concerning the respective radial displacements.

$$\begin{bmatrix} F_x \\ F_y \end{bmatrix} = \begin{bmatrix} \frac{\partial W_m}{\partial x} \\ \frac{\partial W_m}{\partial y} \end{bmatrix} \quad (2)$$

Given the mechanical rotor speed, denoted as ω_{rm} , while $\theta_{rm} = \int \omega_{rm} dt$, slip frequencies can be written as [4].

$$\begin{cases} \omega_{2s} = \omega_2 - \omega_{rm} \\ \omega_{4s} = \omega_4 - 2\omega_{rm} \end{cases} \quad (3)$$

The suspension force matrix is obtained as follows:

$$\begin{bmatrix} F_x \\ F_y \end{bmatrix} = L'_{24} \begin{bmatrix} i_{2as} + i_{2dr} & i_{2\beta s} + i_{2\beta r} \\ -(i_{2\beta s} + i_{2\beta r}) & i_{2as} + i_{2ar} \end{bmatrix} \begin{bmatrix} i_{4as} + i_{4ar} \\ i_{4\beta s} + i_{4\beta r} \end{bmatrix} \quad (4)$$

The parameters i_{2as} , $i_{2\beta s}$, i_{2ar} , $i_{2\beta r}$, i_{4as} , $i_{4\beta s}$, i_{4ar} , and $i_{4\beta r}$ represent steady-state current values. The symbol L'_{24} refers to the mutual inductance between the motoring and force windings. The electromagnetic torque can be described by the following equation, where L_{2s} is the inductance of the motoring winding and L_{4s} is the force winding inductance [22].

$$T_e = \frac{\partial W_{mech}}{\partial x} = L_{2s}(i_{2ar}i_{2\beta s} - i_{2as}i_{2\beta r}) + L_{4s}(i_{4ar}i_{4\beta s} - i_{4as}i_{4\beta r}) \quad (5)$$

Table I. Parameters of the BLIM

Parameter	Symbol	Constraints
Power of the motor	P	2200 W
Nominal speed	N	30000 rpm
Poles of torque winding	P_t	2
Poles of force winding	P_f	4
Frequency	f	250 Hz
Slots in stator	Q_s	30
Slots in rotor	Q_r	24
Nominal voltage	V_L	220 V
Current in torque	I_t	10 A
Current in force	I_s	5 A
Stack length	l	38 cm

Rotor slot depth	h_{rp}	2.5 cm
Fill factor of stator slot	f_f	0.6

3. Optimization

3.1. Multi Objective Optimization Problem (MOOP)

In this paper, \underline{x} denotes decision vectors. The objective function $\underline{\psi}(\underline{x})$ is formulated as $\underline{\psi}(\underline{x}) = \{\psi_1(\underline{x}), \psi_2(\underline{x}), \dots, \psi_q(\underline{x})\}$. The algorithm aims to replace a group of non-dominated solutions with an optimized one. The primary objective is to minimize the MOOP value, which requires minimizing the individual objective functions accordingly.

$$\text{Minimize } \underline{\psi}(\underline{x}) = \{\psi_1(\underline{x}), \psi_2(\underline{x}), \dots, \psi_n(\underline{x})\} \quad (6)$$

In the context, ψ_i represents the i^{th} objective function, and \underline{x} denotes the state within an N -dimensional decision space. BLIM exhibits a distinct structure and performance characteristics more intricate than traditional induction motors. The concurrent effects of torque and force production units can detrimentally impact motor performance. To optimize BLIM dimensions, an effective objective function incorporating optimization parameters needs to be established. This includes prioritizing optimization of average suspension force (F_{av}), average electromagnetic torque (T_{av}), and force ripple (RF). Introducing x as adjustable parameters, the objective function is defined based on these specified criteria.

$$\varphi_1(\underline{x}) = \frac{1}{F_{av}} \quad (7)$$

$$\varphi_2(\underline{x}) = \frac{1}{T_{av}} \quad (8)$$

$$\varphi_3(\underline{x}) = RF \quad (9)$$

Furthermore, the weight of a motor plays a crucial role in its applications. In this study, the third objective function is specifically defined as the total weight of the motor.

$$\varphi_4(\underline{x}) = M \quad (10)$$

To achieve minimal objective functions, it is necessary to optimize suitable variable parameters. Certain motor dimensions are interdependent, complicating the optimization process when both parameters need selection. In this study, the optimization parameters are defined as shown in Fig. 5.

The motor design method proposed in [18] was utilized to establish initial dimensions, which serve as the starting point for optimization. Some dimensions obtained initially are excluded from the optimization process and listed in Table I alongside other unchanged parameters. This section details the optimization of the designed BLIM using the MOOP method. Adjustable parameters are specified in Fig. 4. Therefore, parameter \underline{x} can be chosen as follows:

$$\underline{x} = (g, w_{sp}, w_{rp}, h_{sp}, h_{rp}, h_{s0}, h_{r0}, h_{sy}, \theta_{sp}, \theta_{rp}) \quad (11)$$

The parameters chosen for optimization are constrained within specific ranges to prevent overlap. The motor's

adjustable dimensions within predefined intervals are detailed in Table II.

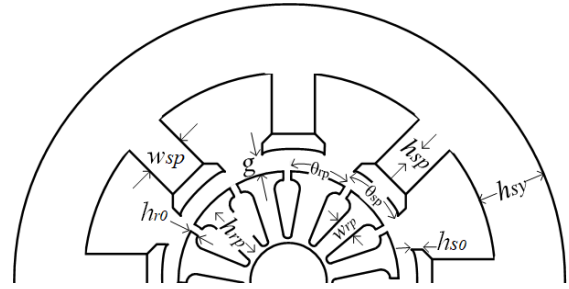


Fig. 5. The optimization parameters of the BLIM,

Table II. Adjustable dimensions of the BLIM

Symbol	Constraints
g	0.2 – 2 mm
w_{sp}	0.3 – 5 mm
w_{rp}	5 – 10 mm
h_{sp}	14 – 20 mm
h_{s0}	1 – 4 mm
h_{r0}	1 – 4 mm
h_{sy}	30 – 45 mm
θ_{sp}	2 – 5 deg
θ_{rp}	2 – 6 deg

During each optimization phase, the suspension force, electromagnetic torque, force ripple, and total motor mass are assessed across a range of x values. Optimization proceeds until achieving the minimum of objective function (12). This multi-objective optimization process is formulated as:

$$f = \min \{\varphi_1, \varphi_2, \varphi_3, \varphi_4\} \quad (12)$$

3.2. Seeker Optimization Algorithm

The Seeker Optimization Algorithm (SOA) is a novel strategy for real-parameter optimization that simulates human behavior by incorporating memory, experience, and uncertainty. The algorithm operates on a population of seekers, each contributing to the search for optimal solutions. Multi-optimization is achieved through the collaboration of these seekers, who are divided into distinct sub-populations to explore different search spaces.

The initialization processes

Initially, a set of initial seekers is defined based on the motor's initial design. Each seeker comprises D dimensions, corresponding to the adjustable parameters of the machine structure. These dimensions are randomized to optimize the adjustable aspects of the BLIM, aiming to generate a set of viable solutions within given constraints. Subsequently, a rapid non-dominated sorting algorithm selects the best individual from a current population of size N_i . To facilitate information sharing, each seeker is assigned a neighborhood. The main population is divided into K sub-populations, each containing a group of seekers that form a neighborhood of identical size.

The search processes

Assuming \underline{x} in equations (7) to (10) represents a set of adjustable parameters, the position of the k^{th} seeker at iteration t can be expressed as $\underline{x}_k(t) = [x_{k1}, x_{k2}, \dots, x_{kj}, \dots, x_{kM}]$. Here, t denotes the iteration number, while j and M refer to the j^{th} dimension and the total number of parameters associated with each dimension, respectively. To update the j^{th} component of the j^{th} seeker's position, $\vec{a}_i(t) \geq 0$ and $\vec{\lambda}_i(t) \in \{-1.0.1\}$ are defined for step length and search direction.

$$x_k(t+1) = x_k(t) + \vec{\beta}_k(t)\vec{\lambda}_k(t) \quad (13)$$

Table III presents the equations corresponding to different $\vec{a}_i(t)$ values, each satisfying $\vec{a}_i(t) \geq 0$. Each subpopulation conducts its search independently using its own data, which may lead to convergence at local optima.

Table III. Different values of $\lambda_k(t)$

Value	Action
$\lambda_k(t) = -1$	Move to the opposite direction
$\lambda_k(t) = 0$	Remain at the current position
$\lambda_k(t) = 1$	Move to the positive direction

To mitigate this, the current position of the n^{th} worst member in the i^{th} subpopulation ($x_{inj.worst}$) is identified and replaced by the best position found in the q^{th} subpopulation ($x_{qj.best}$).

$$x_{inj.worst} = \begin{cases} x_{qj.best} & \text{if } R_j \leq 0.5 \\ x_{inj.worst} & \text{else} \end{cases} \quad (14)$$

The proposed optimization algorithm involves seekers progressing through their search with an empirical gradient. This method employs multiple empirical gradients to establish the search direction by comparing the seeker's current and previous positions. The direction of search is determined based on personal, local, and global directions, as well as historical trends and step length.

Personal direction

Each individual in a population constantly aims to reach their highest achieved position ($\vec{\rho}_{k.best}(t)$). If $\vec{x}_k(t)$ represents the current position of individual k , the direction of search can be described as follows.

$$\vec{\lambda}_{k.ego}(t) = \text{sign}(\vec{\rho}_{k.best}(t) - \vec{x}_k(t)) \quad (15)$$

Local and global directions

These are determined through collaboration among group elements. The primary population is divided into K groups, each containing an equal number of seekers. The local best position ($\vec{\lambda}_{k.local}(t)$) refers to the optimal position of a seeker within a sub-population, while the global best position ($\vec{\lambda}_{k.global}(t)$) denotes the best position among all sub-populations.

$$\vec{\lambda}_{k.local}(t) = \text{sign}(\vec{g}_{k.best}(t) - \vec{x}_k(t)) \quad (16)$$

$$\vec{\lambda}_{k.global}(t) = \text{sign}(\vec{q}_{k.best}(t) - \vec{x}_k(t)) \quad (17)$$

where $\vec{g}_{k.best}(t)$ and $\vec{q}_{k.best}(t)$ represent the current local and global best positions, respectively.

Historical direction

A universal solution, coupled with accumulated past experiences during the search process, enables a seeker to optimize their memory's best outcomes. Consequently, each seeker may pursue distinct search paths, selecting targeted strategies based on their optimal performance. The empirical or proactive direction ($\vec{\lambda}_{k.pro}(t)$) is defined using the positions $\vec{x}_k(t_1)$ and the improved position $\vec{x}_k(t_2)$ as follows:

$$\vec{\lambda}_{k.pro}(t) = \text{sign}(\vec{x}_k(t_1) - \vec{x}_k(t_2)) \quad (18)$$

where t_1, t_2 can be $t, t-1$, or $t-2$. The j^{th} component of the search direction for the k^{th} seeker can be determined using equation (19).

$$\lambda_{kj} = \begin{cases} 0 & \text{if } d_j \leq \rho_j^{(0)} \\ +1 & \text{if } \rho_j^{(0)} < d_j \leq \rho_j^{(0)} + \rho_j^{(+1)}, \\ -1 & \text{if } \rho_j^{(0)} + \rho_j^{(+1)} < d_j \leq 1 \end{cases}$$

$$\rho_j^{(m)} = \frac{\text{num}^m}{4}. \quad (m \in \{0.1, -1\}) \quad (19)$$

Where $d_j \in [0, 1]$, num^m and $\rho_j^{(m)}$ denote the number of m and it's percent for each dimension j of all the four empirical directions, respectively.

Step length

In the proposed optimization algorithm, the step length is determined using fuzzy logic, which captures the uncertain reasoning inherent in human search. Seekers are ranked in descending order based on their fitness values, serving as inputs to the fuzzy logic system. This system employs linear membership functions defined by maximum (μ_{max}) and minimum (μ_{min}) values. Once the seekers are sorted by fitness, the linear membership function for $x_k(t)$ can be formulated as follows:

$$\mu_k = \mu_{max} - \frac{s-I_k}{s-1}(\mu_{max} - \mu_{min}). \quad \mu_{max} \leq 1 \quad (20)$$

where, I_k represents the sequence number. To determine fuzzy sets and control rules, popular bell membership function $f(x) = e^{-x^2/2\sigma^2}$ is used in this work with $\mu_{max} = 0.96$ and $\mu_{min} = 0.012$. Parameter σ for the best seeker position \vec{x}_{best} and random seeker \vec{x}_{rand} is obtained using (21).

$$\sigma = \gamma \cdot |x_{best} - x_{rand}| \quad (21)$$

In the algorithm, ω is set to 0.9. Equation (22) is employed to transform the parameter μ_i into a vector, aiming to improve local search capabilities and account for parameter randomness.

$$\mu_k = \text{rand}(\mu_k, 1) \quad (22)$$

The value $\text{rand}(\mu_k, 1)$ lies within the interval $[\mu_i, 1]$. For the k^{th} seeker, the step length is determined using the action component of fuzzy logic as follows.

$$\beta_k = \sigma_k \cdot \sqrt{-\text{Ln}(\mu_{kj})} \quad (23)$$

3.3. Optimization of the BLIM

Initially, utilizing primary seekers and considering all constraints listed in Table II, 200 potential configurations

and dimensions for the proposed BLIM are identified. The seeker population is then partitioned into several sub-groups of equal size. Fitness values are computed and seekers are ranked accordingly. Subsequently, the best personal, local, and global positions, along with the components of the search direction, are determined. Equation (13) is applied to update seeker positions for selecting better positions. Following the application of the non-dominated sorting process, the top N seekers are selected from the set of seeker movements for the next iteration. Utilizing a non-dominated fast sorting algorithm, the best set of N seekers is derived by merging current and previous solutions. This iterative process continues until the algorithm's termination condition is satisfied.

4. Evaluation of Results

The BLIM design was based on the analytical approach outlined in [18]. Initial dimensions were achieved and subsequently optimized using the (SOA) method, resulting in the dimensions reported in Table IV. 3-D finite element analysis of the motor was conducted using ANSYS Electronics software, with results extracted for precise evaluation. Additionally, a genetic algorithm-based optimization approach (NSGA III) described in [25] was applied to the motor. A comparative analysis was performed among the initial design, the NSGA III optimized design, and the proposed optimized design. The levitation forces in the F_x and F_y axes were evaluated. Under normal conditions, when the rotor is centered on the axis, only F_y is active to maintain rotor position, while F_x remains inactive. If the rotor deviates from center, an appropriate force is generated to recenter it. The suspension force corresponding to different rotor distances from the center is shown in Fig. 6.

Fig. 7 illustrates the variations of average suspension force and average torque concerning the force winding current, across different values of torque current (I_t). The curves demonstrate a direct correlation between average force and force winding current. For a more comprehensive analysis, rated currents are applied to both torque and force windings with varying current phase angles (λ). The results are depicted in Fig. 8. As shown in Fig. 8(b), F_x and F_y follow sine and cosine curves, respectively. This figure illustrates how the forces in two directions contribute to the resultant suspension force vector. Adjusting the winding currents enables control over the direction of the suspension force.

Table IV. Initial and optimized parameters of the BLIM

Symb	Initial	NSGA-III	Proposed
g	1 mm	0.9 mm	0.9 mm
w_{sp}	3 mm	3.5 mm	3.3 mm
w_{rp}	6 mm	6.4 mm	6.8 mm
h_{sp}	18 mm	17.1 mm	16.6 mm
h_{s0}	2 mm	2.2 mm	2.1 mm
h_{r0}	2 mm	2 mm	1.6 mm
h_{sy}	40 mm	34 mm	36.5 mm
θ_{sp}	3.6 deg	3.6 deg	3.55 deg
θ_{rp}	3.9 deg	4.2 deg	3.95 deg

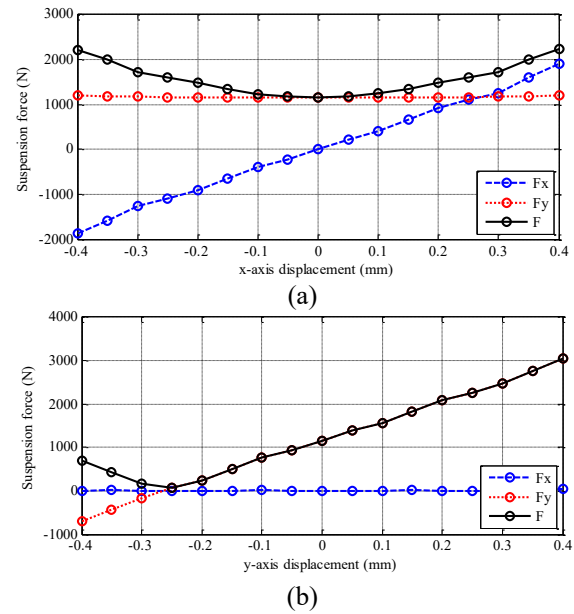


Fig. 6. 2-D suspension forces via two axes displacement, (a) x-direction displacement, (b) y-direction displacement.

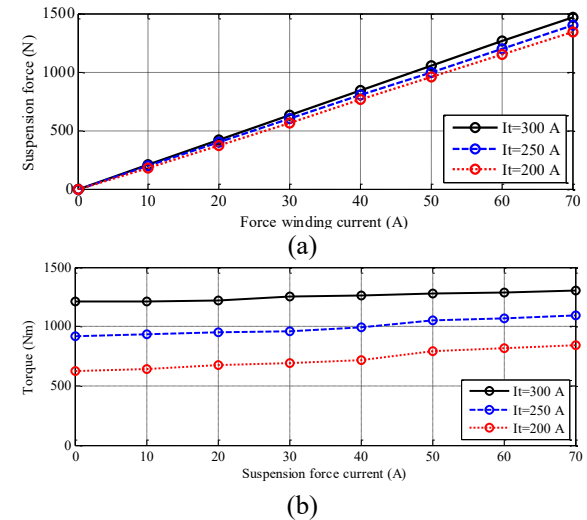


Fig. 7. (a) suspension force, (b) torque, in different force currents.

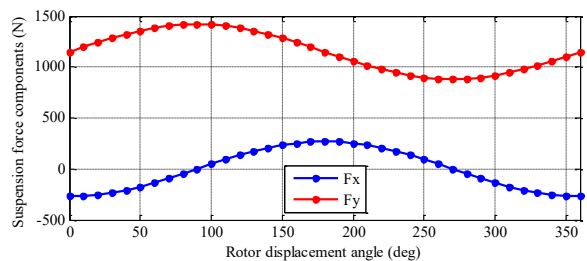


Fig. 8. Suspension force, F_x and F_y .

During operation, external disturbances may cause displacement of the rotor from the center. It is essential to minimize the impact of this displacement on the BLIM's performance. Fig. 9 illustrates the output torque quality under rated torque and force windings currents to assess this situation. The curves indicate minimal changes in the optimized BLIM compared to the other two structures.

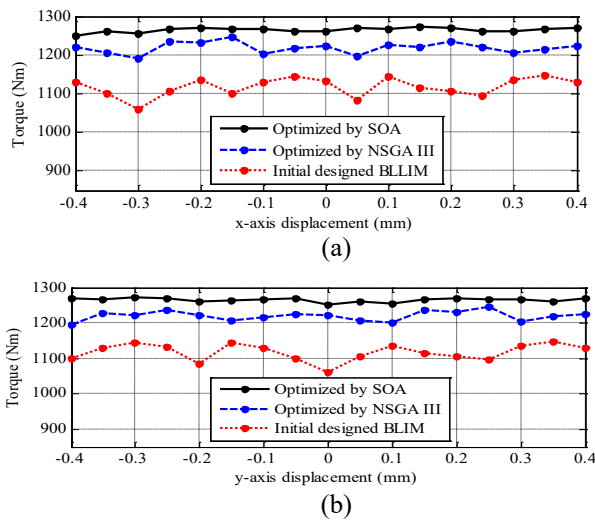


Fig. 9. Electromagnetic torque with respect to (a) x-axis displacement (b) y-axis displacement.

5. Conclusion

In this work, new high-speed high-power bearing-less induction motor (BLIM) was designed and optimized for oil and gas industry applications. The proposed motor generates a two pole electromagnetic field for torque and another four pole one for suspension force as magnetic bearing. The motor consists of a conventional stator along with a special multi two pole rotors. This structure significantly eliminates the adverse effects of two fields on each other and thus increases the efficiency of the BLIM. In order to achieve a better structure, an appropriate objective function consisting of average torque, average suspension force, force ripple, and total weight of the motor was defined and the BLIM optimization was done based on seeker optimization algorithm. 3-D finite element analysis of the motor was done in *ANSYS ELECTRONICS* software and its performance was studied under different speed, load, and displacement conditions.

6. References

- [1] A. Chiba, T. Fukao, O. Ichikawa, M. Oshima, M. Takemoto, and D. G. Dorrel, "Magnetic bearings and bearingless drives," *Liacre House, Joordan Hill. Oxford OX2 8DP, 30 Corporate Drive, Burlington, MA 01803*.
- [2] J. Chen, J. Zhu, E. L. Severson, "Review of bearingless motor technology for significant power application," *IEEE Trans. Ind. Appl.*, vol. 56, no. 2, pp. 1377-1388, 2021.
- [3] T. Pei, D. Li, J. Liu, J. Li, W. Kong, "Review of bearingless synchronous motors: principle and topology," *IEEE Trans. Trans. Electrification*, vol. 8, no. 3, pp. 3489-3502, 2022.
- [4] T. Hiromi, T. Katou, A. Chiba, M. A. Rahman, T. Fukao, "A novel magnetic suspension-force compensation in bearingless induction motor drive with squirrel cage rotor," *IEEE Trans. Ind. Appl.*, vol. 43, no. 1, pp. 66-77, 2007.
- [5] T. Tera, Y. Yamauchi, A. Chiba, T. Fukao, M. A. Rahman, "Performances of bearingless and sensorless induction motor drive based on mutual inductances and rotor displacements estimation," *IEEE Trans. Ind. Elec.*, vol. 53, no. 1, pp. 187-195, 2006.
- [6] H. Mitterhofer, B. Mrak, and W. Gruber, "Comparison of high-speed bearingless drive topologies with combined windings," *IEEE Trans. Ind. Appl.*, vol. 51, no. 3, pp. 2116-2122, 2015.
- [7] D. Steinert, T. Nussbaumer, and J. W. Kolar, "Concept of a 150 krpm bearingless slotless disc drive with combined windings," *IEEE Int. Electric Mach. Drives Conf.*, pp. 311-318, 2013.
- [8] J. Chen, Y. Fujii, M. W. Johnson, A. Farhan, and E. L. Severson, "Optimal design of the bearingless induction motor," *IEEE Trans. Ind. Appl.*, vol. 57, no. 2, pp. 1375-1389, 2021.

- [9] Y. Jiang and E. L. Severson, "Floating capacitor suspension inverter for parallel combined winding bearingless motors," *IEEE Trans. Ind. Appl.*, vol. 56, no. 2, pp. 1518-1528, 2020.
- [10] W. Khoo, K. Kalita, and S. Garvey, "Practical implementation of the bridge configured winding for producing controllable transverse forces in electrical machines," *IEEE Trans. Mag.*, vol. 47, no. 6, pp. 1712-1718, 2011.
- [11] R. Oishi, S. Horima, H. Sugimoto, and A. Chiba, "A novel parallel motor winding structure for bearingless motors," *IEEE Trans. Mag.*, vol. 49, no. 5, pp. 2287-2290, 2013.
- [12] E. L. Severson, S. Gandikota, and N. Mohan, "Practical implementation of dual-purpose no-voltage drives for bearingless motors," *IEEE Trans. Ind. Appl.*, vol. 52, no. 2, pp. 1509-1518, 2016.
- [13] R. Abebe, M. D. Nardo, D. Gerada, G. L. Calzo, L. Papini, and C. Gerada, "High-speed drives review: machines, converters and applications," *IECON 42nd Annual Conf., IEEE Ind. Elec. Society*, 2016.
- [14] P. Beer, J. E. Tessaro, B. Eckels, and P. Geberson, "High-speed motor design for gas compressor applications," *Proceedings of the thirty-fifth turbomachinery symposium*, 2006.
- [15] T. Noguchi, W. Chan, N. Petersen, L. Rapp, E. Severson, "Opportunities to Enhance sCO₂ Power Cycle Turbomachinery with Bearingless Motor/Generators," *Solar Compass*, vol. 12, pp. 706-714, 2024.
- [16] W. Xiaoyuan, L. Na, L. Tianyuan, X. Yuhao, "Electromagnetic design of an ultra-high-speed bearingless permanent magnet synchronous motor," *IET Electric Power Appl.*, vol. 18, no. 3, 2024.
- [17] K. Krishnan, E. Severson, M. Noh, W. Gruber, "Bearingless Motors: Fundamentals and Current Status," *IEEE Energy Conversion Congress and Expo*, Phoenix, Arizona, USA, Oct. 20-24, 2024.
- [18] A. Khamitov, E. L. Severson, "Multiharmonic Force Vector Model for Bearingless Electric Motors," *IEEE Trans. On Industry App.*, vol. 61, no. 1, 2025.
- [19] C. Lu, Z. Yang, X. Sun, Q. Ding, "Modelling and optimization for a special pole bearingless induction motor," *Engineering Optimization*, vol. 55, no. 10, 2023.
- [20] K. Li, G. C. X. Sun, Z. Yang, and Y. Fan, "Performance optimization design and analysis of bearingless induction motor with different magnetic slot wedges," *Results in Physics*, vol. 12, pp. 349-356, 2019.
- [21] J. Chen, J. Zhu, and E. L. Severson, "Review of bearingless motor technology for significant power applications," *IEEE Trans. Ind. Appl.*, vol. 56, no. 2, pp. 1377-1388, Mar./Apr. 2020.
- [22] X. Ye, Z. Yang, T. Zhang, "Modelling and performance analysis on a bearingless fixed-pole rotor induction motor," *IET Elec. Power Appl.*, vol. 13, no. 2, pp. 259-266, 2019.
- [23] U. C. Hasar, Y. Kaya, H. Korkmaz, T. Lliev, "Broadband Multilayer Absorber Design Using Double-Stage Cognitive Seeker Optimization Algorithm," *IEEE Access*, vol. 13, no. 2, pp. 27178-27190, 2025.
- [24] M. Soltanpour, H. Abdollahi, and S. Masoudi, "Optimisation of Double Sided Linear Switched Reluctance Motor for Mass and Force Ripple Minimization," *IET Science, Measurement and Technology*, vol. 13, no. 4, pp. 509-517, 2019.
- [25] A. Wu, R. Gong, J. Mao, X. Yu, J. He, "Voltage Feed-Forward Control of Photovoltaic- Battery DC Microgrid Based on Improved Seeker Optimization Algorithm," *IEEE Access*, vol. 12, 2025.